SUPPORTING INFORMATION

Chinese Journal of Structural Chemistry

# Explicating the Role of Metal Centers in Porphyrin-Based MOFs of PCN-222(M) for Electrochemical Reduction of $CO_2$

Mengjie Liu[1†], Mengting Peng[1†], Baoxia Dong[1*], Yunlei Teng[1], Ligang Feng[1] and Qiang Xu[1*]

[1]*School of Chemistry and Chemical Engineering, Yangzhou University, Yangzhou, Jiangsu 225002, China*

*Corresponding authors. E-mails: bxdong@yzu.edu.cn (B. X. Dong), qxuchem@yzu.edu.cn (Q. Xu)*

*† These authors contributed equally to this work.*

# SUPPORTING INFORMATION

Chinese Journal of Structural Chemistry

## n TABLE OF CONTENTS

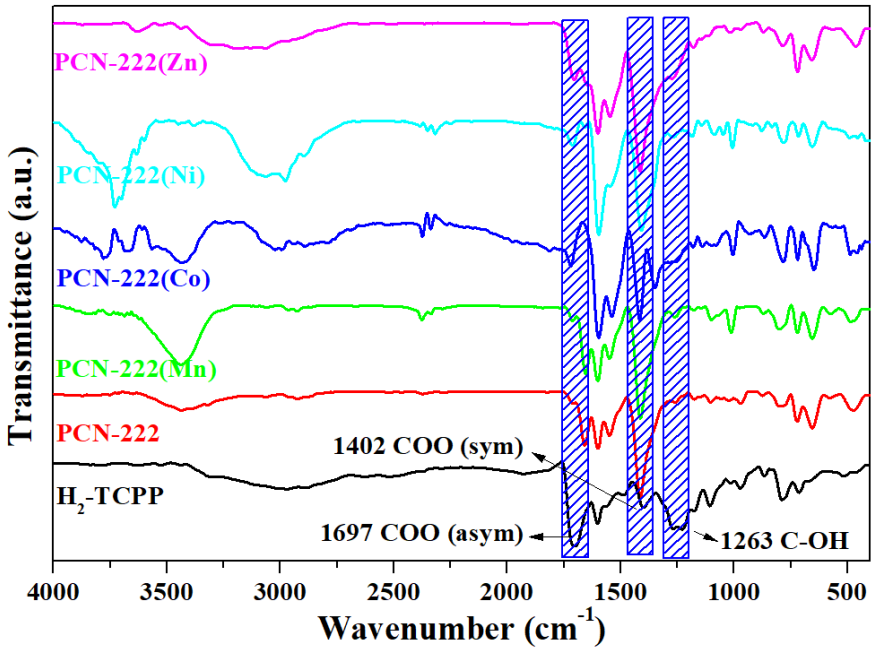


**Figure S1.** IR spectrum of each catalyst.

The stretching vibrations at 1697 and 1263 $cm^{-1}$ in $H_2$-TCPP can be attributed to the COO (asymmetric) and -OH groups. Those intensities in PCN-222 decreased significantly, indicating the coordination interaction between the -COOH group and $Zr_6$ cluster. Moreover, the intensity of COO (symmetric) at 1407 $cm^{-1}$ in PCN-222 enhanced significantly (vs. 1402 $cm^{-1}$ in $H_2$-TCPP).[1-3]

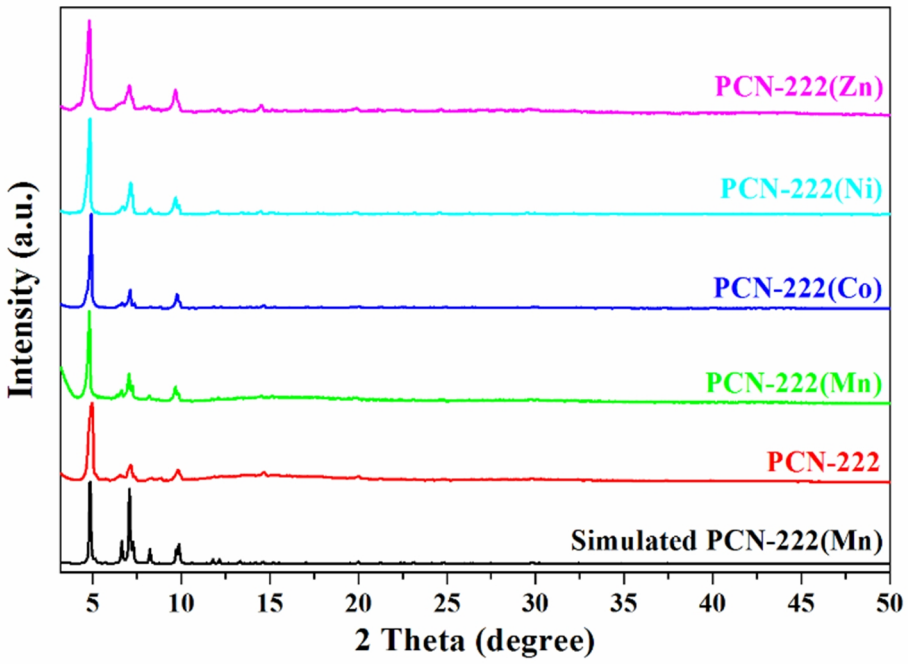


**Figure S2.** PXRD patterns of PCN-222 and PCN-222(M), M = Mn, Co, Ni, Zn.

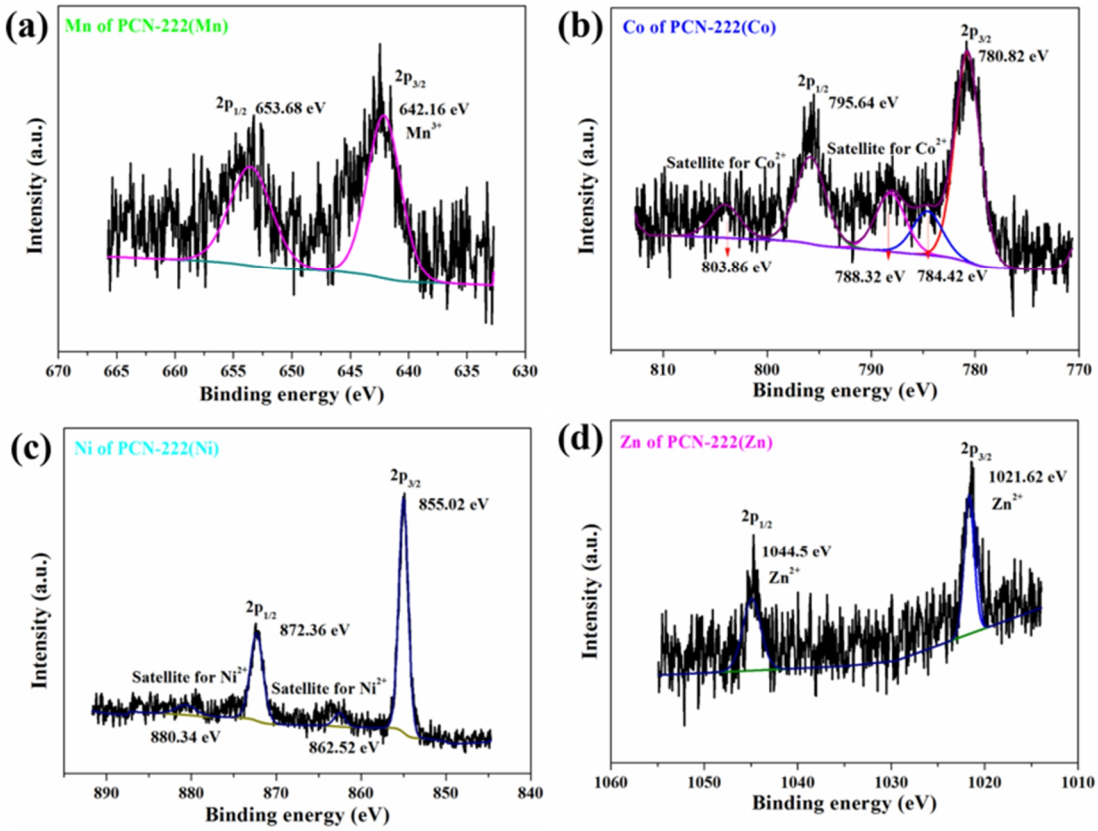


**Figure S3.** XPS of (a) Mn 2p; (b) Co 2p; (c) Ni 2p; (d) Zn 2p.

As depicted in Figure S3, the high-resolution Mn 2p spectra of PCN-222(Mn) are fitted into two peaks at 642.16 and 653.68 eV, which are attributed to Mn $2p_{3/2}$ and Mn $2p_{1/2}$ for $Mn^{3+}$, respectively.[4,5] For PCN-222(Co), the peaks at 780.82 and 795.64 eV are fitted into Co $2p_{3/2}$ and Co $2p_{1/2}$ for $Co^{2+}$, respectively.[5-7] The peaks of Ni $2p_{3/2}$ and Ni $2p_{1/2}$ attributable to $Ni^{2+}$ for PCN-222(Ni) are at 855.02 and 872.36 eV, respectively.[7,8] Similarly, the peaks of PCN-222(Zn) located at 1021.62 and 1044.50 eV are attributed to the Zn $2p_{3/2}$ and Zn $2p_{1/2}$ for $Zn^{2+}$, respectively.[9]

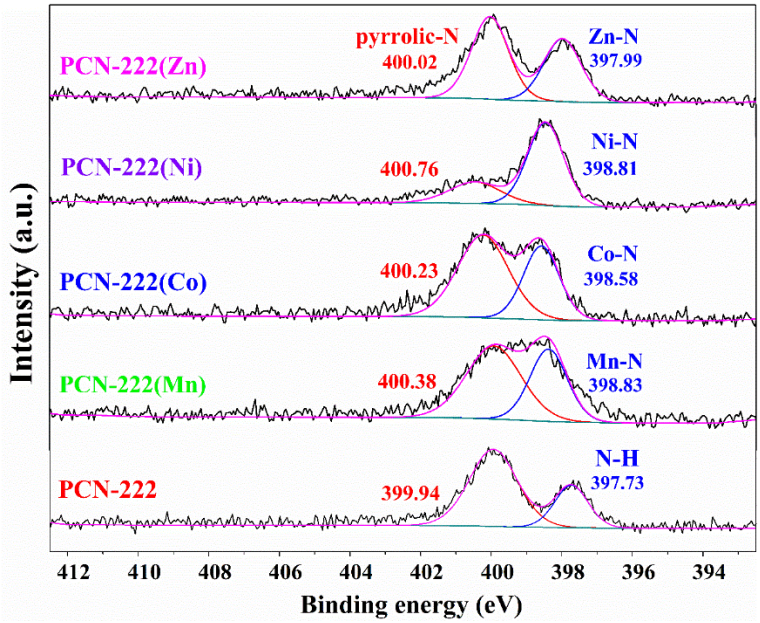


**Figure S4**. XPS of N1s for PCN-222(M), M = Mn, Co, Ni, Zn.

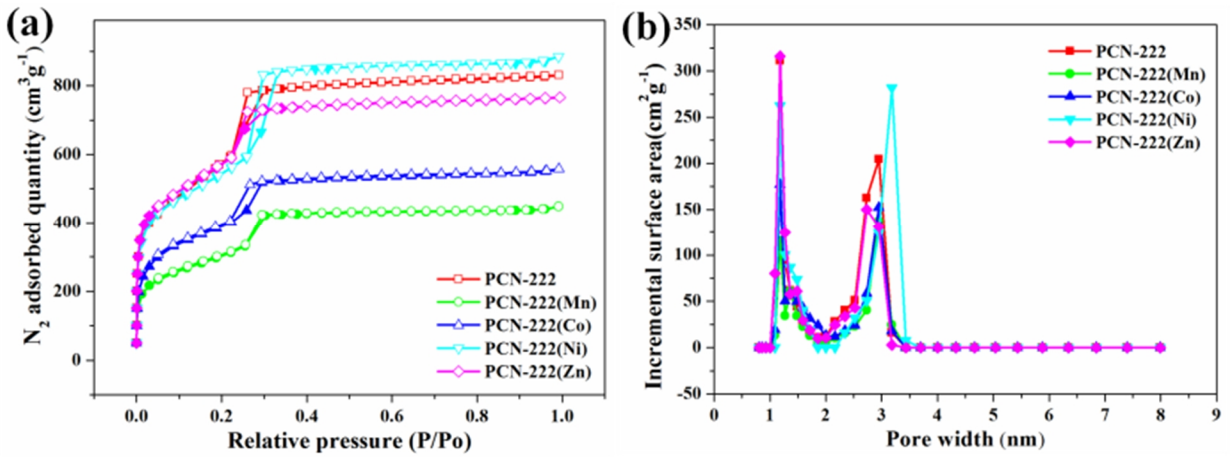


**Figure S5.** (a) $N_2$ sorption isotherms at 77 K, solid, adsorption; hollow, desorption; (b) DFT pore size distribution of PCN-222 and PCN-222(M).

**Table S1.** $S_{BET}$ and $V_{pore}$ of Each Catalyst

| | PCN-222 | PCN-222(Mn) | PCN-222(Co) | PCN-222(Ni) | PCN-222(Zn) |
|---|---|---|---|---|---|
| $S_{BET}$ ($m^2\ g^{-1}$) | 2410 | 1230 | 1543 | 2017 | 2247 |
| $V_{pore}$ ($cm^3\ g^{-1}$) | 1.29 | 0.69 | 0.86 | 1.37 | 1.19 |
| Reported [10] | 2223 | 2045 | 1864 | 2283 | 1906 |

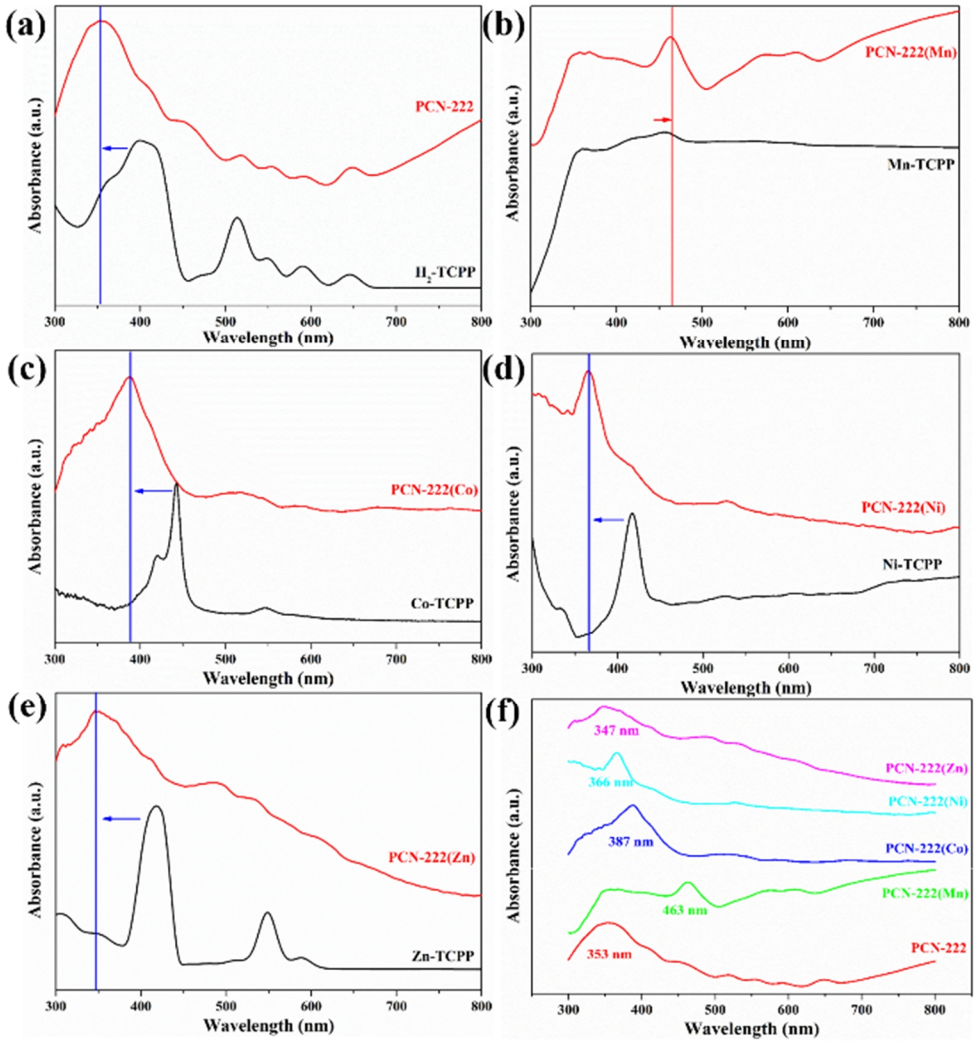


**Figure S6**. UV-vis spectra of (a) PCN-222 and $H_2$-TCPP; (b-e) PCN-222(M) and M-TCPP in $CH_2Cl_2$; (f) Illustration of the comparison for the extended frameworks.

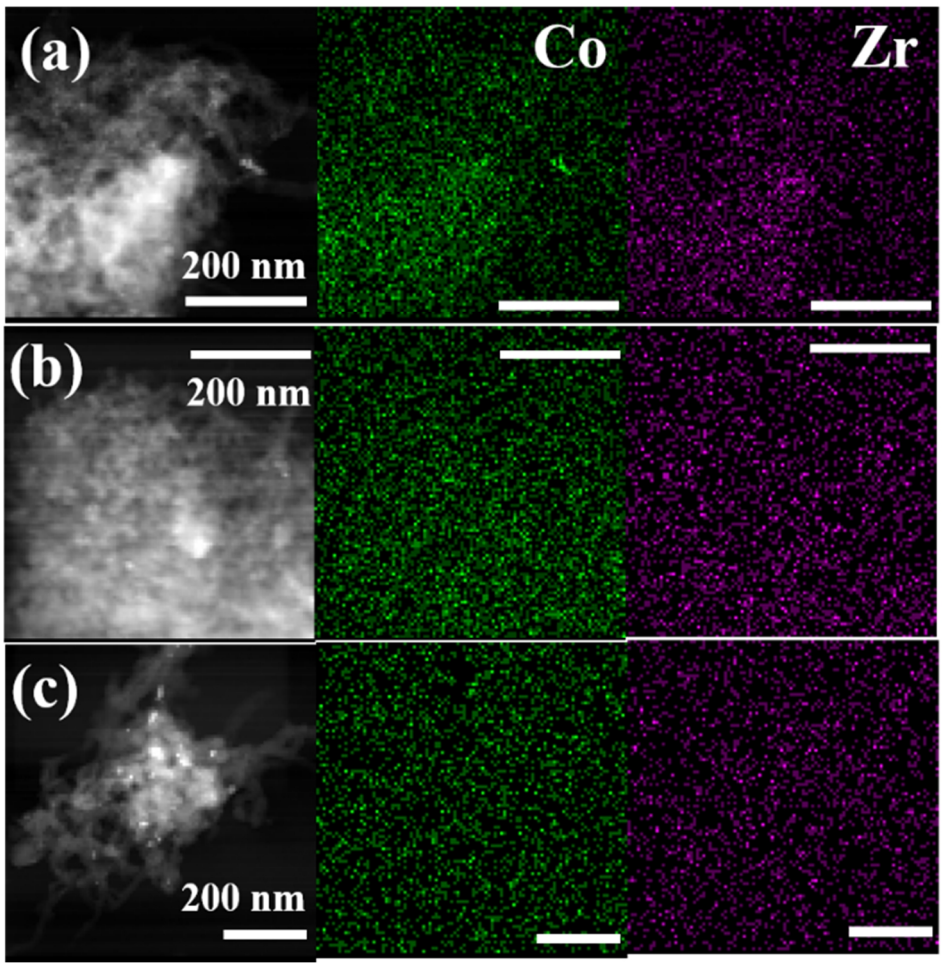


**Figure S7.** HAADF-STEM and EDS elemental (Co, Zr) mapping of PCN-222(Co)/CNT with different catalyst contents: (a) 1:1; (b) 1:10; (c) 1:30.

As depicted in Figure S7, it reveals low contents of Co and Zr even in the high composite ratios of PCN-222/PCN-222(M):CNT = 1:1 and 1:10.

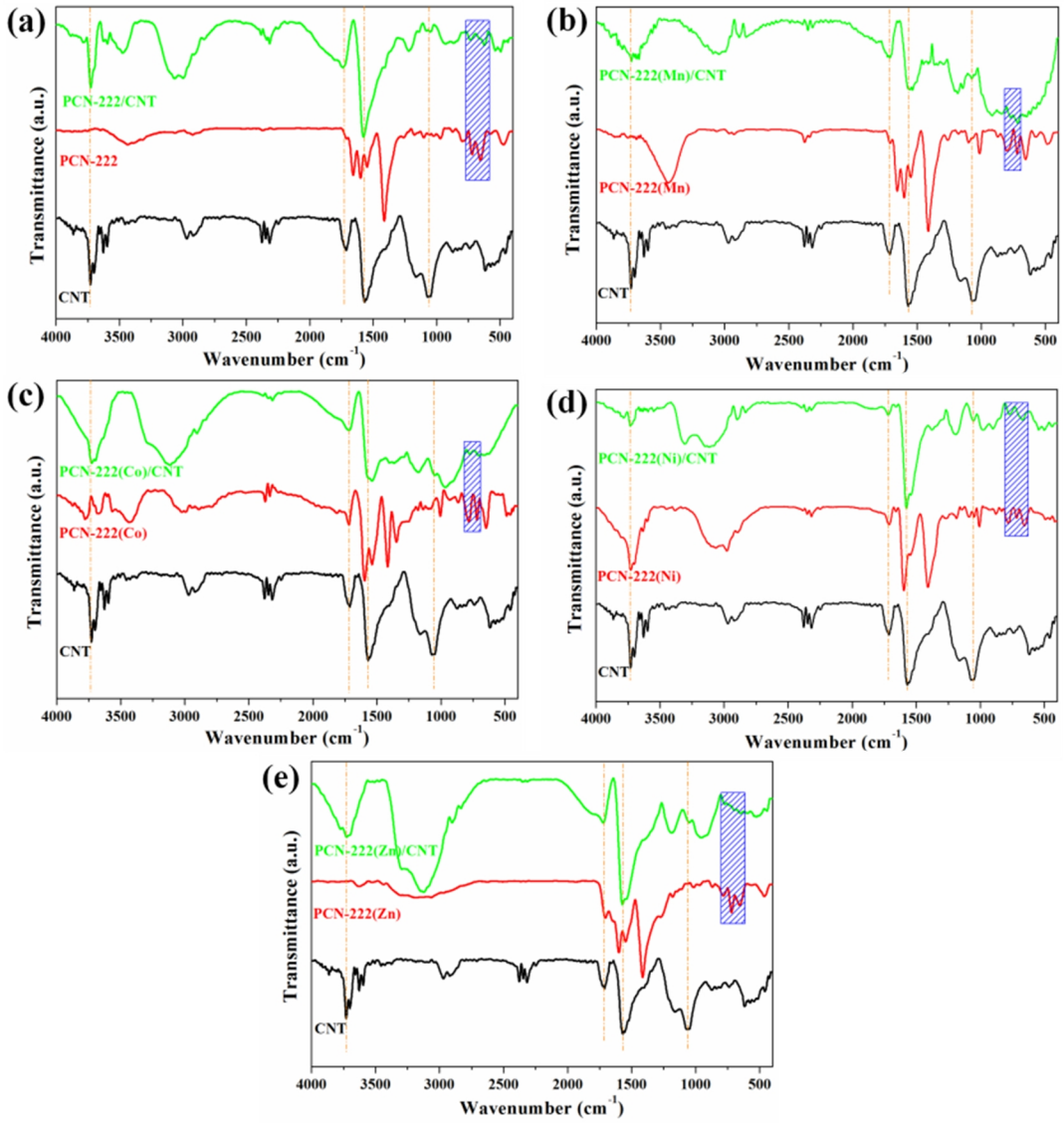


**Figure S8.** IR spectrum of each catalyst.

Take PCN-222/CNT as an example. Since hydroxylated CNT was used to combine with MOF, an absorption peak attributed to -OH is observed at 3726 $cm^{-1}$ in CNT and PCN-222/CNT (Figure S8a). PCN-222/CNT shows a weak peak of COO (symmetric) at 1407 $cm^{-1}$. The weak absorption peaks in the range of 650~800 $cm^{-1}$ are attributed to the C-H out-of-plane bending vibration zone on the benzene ring in PCN-222.

The IR spectra of PCN-222(M)/CNT (Figure S8 b-e) are similar to that of PCN-222/CNT.

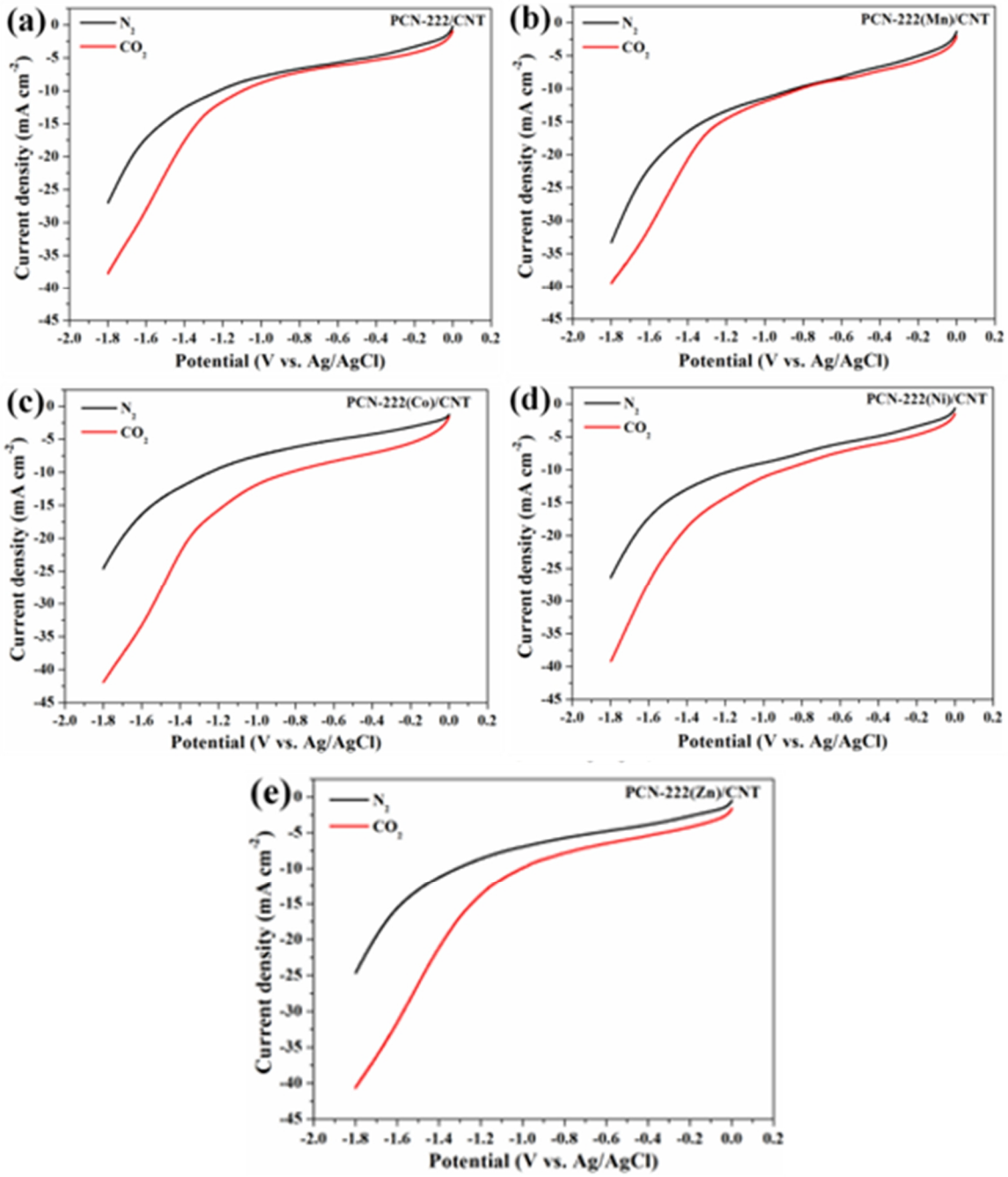


**Figure S9.** LSVs of (a) PCN-222/CNT and (b-e) PCN-222(M)/CNT loaded on CP in $N_2$ and $CO_2$-saturated electrolyte (vs. Ag/AgCl).

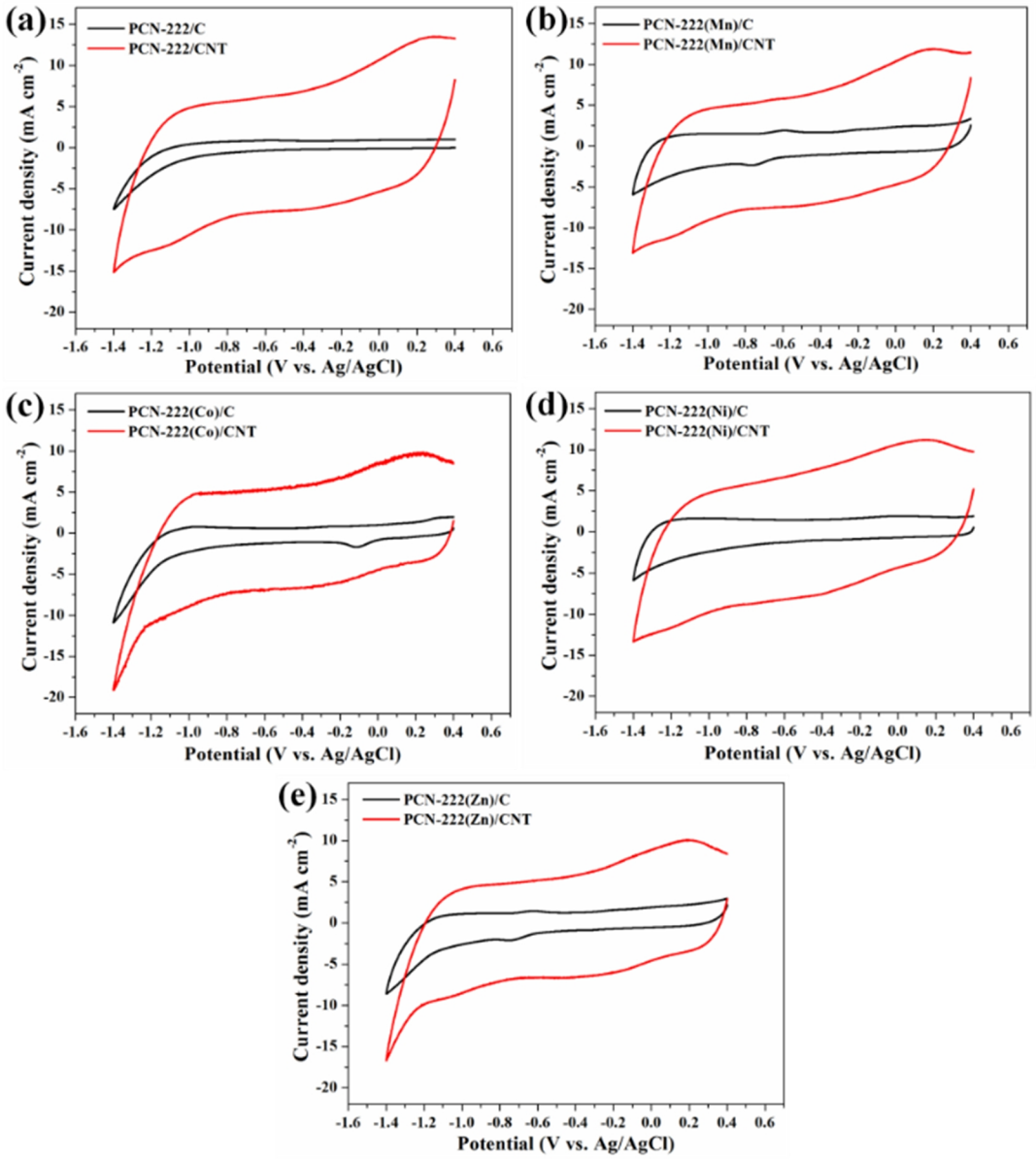


**Figure S10.** CVs of (a) PCN-222/C and PCN-222/CNT; (b-e) PCN-222(M)/C and PCN-222(M)/C NT loaded on CP in $CO_2$-saturated electrolyte (vs. Ag/AgCl).

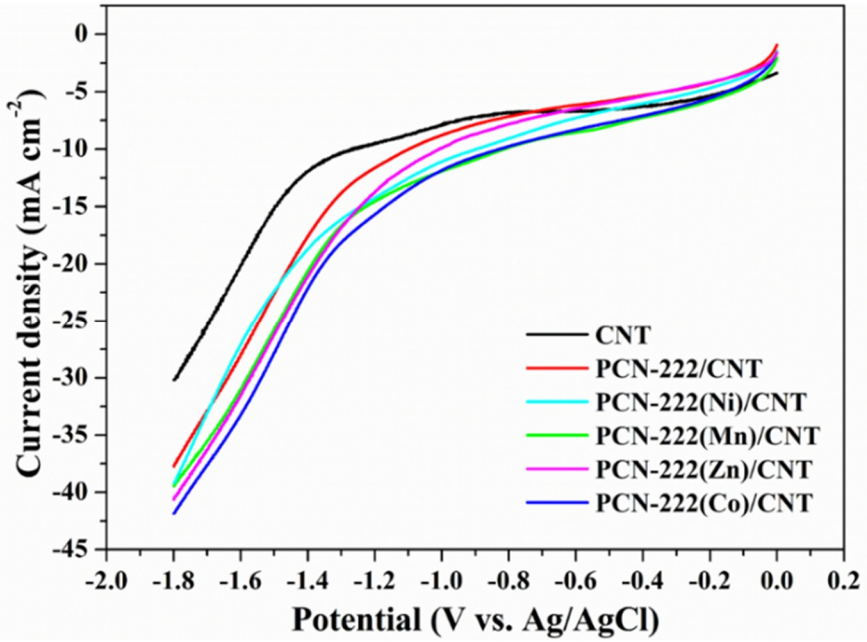


**Figure S11**. Comparison of LSV for each catalyst in the $CO_2$-saturated electrolyte (vs. Ag/AgCl).

**Table S2.** Chronoamperograms and Product Quantified Results for PCN-222/CNT

| vs. Ag/AgCl (V) | -1.135 | -1.185 | -1.235 | -1.285 | -1.335 | -1.385 |
|---|---|---|---|---|---|---|
| vs. RHE (V) | -0.50 | -0.55 | -0.60 | -0.65 | -0.70 | -0.75 |
| $\eta_{CO}$ (mV) | 394 | 444 | 494 | 544 | 594 | 644 |
| *j* (mA $cm^{-2}$) | 0.3 | 0.6 | 0.7 | 0.9 | 1.2 | 1.2 |
| $FE_{H2}$ (%) | 32.3 | 23.2 | 26.1 | 21.9 | 22.4 | 25.4 |
| $FE_{CO}$ (%) | 74.6 | 72.4 | 69.6 | 80.7 | 73.5 | 66.5 |
| TON ($n_{CO}$/n) | 181.1 | 308.4 | 337.5 | 469.2 | 606.8 | 568.4 |
| TOF ($h^{-1}$) | 90.6 | 154.2 | 168.8 | 234.6 | 303.4 | 284.2 |

**Table S3.** Chronoamperograms and Product Quantified Results for PCN-222(Mn)/CNT

| vs. Ag/AgCl (V) | -1.135 | -1.185 | -1.235 | -1.285 | -1.335 |
|---|---|---|---|---|---|
| vs. RHE (V) | -0.50 | -0.55 | -0.60 | -0.65 | -0.70 |
| $\eta_{CO}$ (mV) | 394 | 444 | 494 | 544 | 594 |
| *j* (mA $cm^{-2}$) | 0.3 | 0.6 | 1.1 | 1.3 | 1.7 |
| $FE_{H2}$ (%) | 36.4 | 23.7 | 13.3 | 14.9 | 13.9 |
| $FE_{CO}$(%) | 78.4 | 77.9 | 88.5 | 85.7 | 84.6 |
| TON ($n_{CO}$/n) | 166.8 | 358.9 | 712.6 | 838.7 | 1165.7 |
| TOF ($h^{-1}$) | 83.4 | 179.4 | 356.3 | 419.4 | 582.9 |

**Table S4.** Chronoamperograms and Product Quantified Results for PCN-222(Co)/CNT

| vs. Ag/AgCl (V) | -1.085 | -1.135 | -1.185 | -1.235 | -1.285 | -1.335 | -1.385 |
|---|---|---|---|---|---|---|---|
| vs. RHE (V) | -0.45 | -0.50 | -0.55 | -0.60 | -0.65 | -0.70 | -0.75 |
| $\eta_{CO}$ (mV) | 344 | 394 | 444 | 494 | 544 | 594 | 644 |
| $j$ (mA $cm^{-2}$) | 0.6 | 1.3 | 1.9 | 2.6 | 3.8 | 4.9 | 5.6 |
| $FE_{H2}$ (%) | 41.0 | 36.5 | 27.4 | 23.7 | 12.3 | 16.2 | 16.9 |
| $FE_{CO}$(%) | 65.6 | 68.9 | 77.3 | 80.3 | 89.3 | 85.3 | 80.9 |
| TON ($n_{CO}$/n) | 298.0 | 649.0 | 1142.9 | 1721.0 | 2607.4 | 3033.0 | 3163.6 |
| TOF ($h^{-1}$) | 149.0 | 324.5 | 571.4 | 860.5 | 1303.7 | 1516.5 | 1581.8 |

**Table S5.** Chronoamperograms and Product Quantified Results for PCN-222(Ni)/CNT

| vs. Ag/AgCl (V) | -1.135 | -1.235 | -1.335 | -1.385 | -1.435 | -1.485 | -1.535 |
|---|---|---|---|---|---|---|---|
| vs. RHE (V) | -0.50 | -0.60 | -0.70 | -0.75 | -0.80 | -0.85 | -0.90 |
| $\eta_{CO}$ (mV) | 394 | 494 | 594 | 644 | 694 | 744 | 794 |
| *j* (mA $cm^{-2}$) | 0.1 | 0.1 | 0.3 | 0.7 | 0.8 | 1.1 | 1.7 |
| $FE_{H2}$ (%) | 101.7 | 99.5 | 75.5 | 59.3 | 42.0 | 39.8 | 45.7 |
| $FE_{CO}$(%) | / | 6.0 | 31.4 | 42.8 | 52.0 | 49.4 | 43.9 |
| TON ($n_{CO}$/n) | / | 6.6 | 64.2 | 239.7 | 296.2 | 423.5 | 556.3 |
| TOF ($h^{-1}$) | / | 3.3 | 32.1 | 119.8 | 148.1 | 211.8 | 278.2 |

**Table S6.** Chronoamperograms and Product Quantified Results for PCN-222(Zn)/CNT

| vs. Ag/AgCl (V) | -1.135 | -1.185 | -1.235 | -1.285 | -1.335 | -1.385 |
|---|---|---|---|---|---|---|
| vs. RHE (V) | -0.50 | -0.55 | -0.60 | -0.65 | -0.70 | -0.75 |
| $\eta_{CO}$ (mV) | 394 | 444 | 494 | 544 | 594 | 644 |
| *j* (mA $cm^{-2}$) | 0.2 | 0.4 | 0.8 | 1.3 | 1.8 | 2.4 |
| $FE_{H2}$ (%) | 73.4 | 34.9 | 17.0 | 12.04 | 9.2 | 8.3 |
| $FE_{CO}$ (%) | 32.9 | 63.5 | 88.2 | 88.1 | 92.5 | 91.0 |
| TON ($n_{CO}$/n) | 53.0 | 310.2 | 521.5 | 952.4 | 1305.2 | 1795.1 |
| TOF ($h^{-1}$) | 26.5 | 155.1 | 260.8 | 476.2 | 652.6 | 897.6 |

**Table S7.** Chronoamperograms and Product Quantified Results for CNT

| | |
|---|---|
| vs. Ag/AgCl (V) | -1.235 |
| vs. RHE (V) | -0.60 |
| *j* (mA $cm^{-2}$) | 0.7 |
| $FE_{H2}$ (%) | 96.2 |
| $FE_{CO}$ (%) | / |

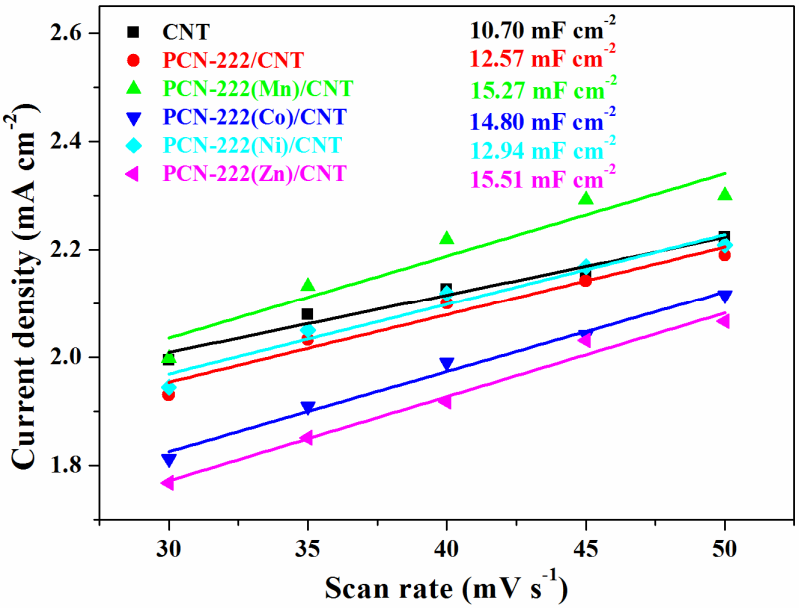


**Figure S12.** Current density plots at various scan rates at -0.75 V vs. Ag/AgCl.

**Table S8.** The Value of $C_{dl}$ and ECSA for Each Catalyst

| Catalyst | $C_{dl}$ (mF $cm^{-2}$) | ECSA ($cm^2$) |
|---|---|---|
| CNT | 10.7 | 535.0 |
| PCN-222/CNT | 12.6 | 628.5 |
| PCN-222(Mn)/CNT | 15.3 | 763.5 |
| PCN-222(Co)/CNT | 14.8 | 740.0 |
| PCN-222(Ni)/CNT | 12.9 | 647.0 |
| PCN-222(Zn)/CNT | 15.5 | 775.5 |

**Table S9.** The Obtained $R_{cell}$ and $R_{ct}$ in Each Catalyst

| Catalyst | $R_{cell}$ (Ω) | $R_{ct}$ (Ω) |
|---|---|---|
| CNT | 3.7 | 31.4 |
| PCN-222/CNT | 4.5 | 44.0 |
| PCN-222(Mn)/CNT | 4.3 | 37.2 |
| PCN-222(Co)/CNT | 3.6 | 10.4 |
| PCN-222(Ni)/CNT | 4.2 | 61.3 |
| PCN-222(Zn)/CNT | 4.8 | 39.6 |

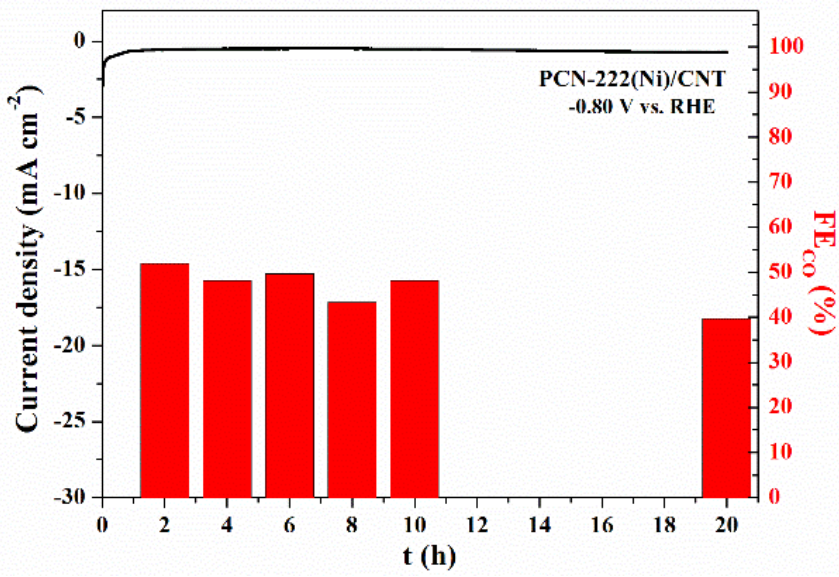


**Figure S13.** Long-term chronoamperometry test (20 h) and Faradaic efficiency for CO as a function of time for PCN-222(Ni)/CNT.

**Table S10.** $FE_{CO}$ at Different Times for Each Catalyst

| Catalyst | 2 h | 4 h | 6 h | 8 h | 10 h | 20 h |
|---|---|---|---|---|---|---|
| PCN-222/CNT | 80.7 | 70.4 | 71.7 | 57.5 | 59.5 | 49.4 |
| PCN-222(Mn)/CNT | 88.5 | 81.4 | 81.0 | 82.4 | 77.9 | 63.1 |
| PCN-222(Co)/CNT | 89.3 | 80.7 | 77.0 | 72.6 | 71.1 | 68.4 |
| PCN-222(Ni)/CNT | 52.0 | 48.2 | 49.6 | 43.3 | 48.2 | 39.7 |
| PCN-222(Zn)/CNT | 92.5 | 95.8 | 85.2 | 89.2 | 83.6 | 67.8 |

**Table S11.** $FE_{CO}$ of Catalysts Containing M-$N_x$ Structure in $CO_2RR$

| Catalyst | Electrolyte | Potential [η] (V) | *j* (mA $cm^{-2}$) | $FE_{CO}$ (%) | Ref. |
|---|---|---|---|---|---|
| PCN-222/CNT | 0.5 M $KHCO_3$ | -0.65 V vs. RHE [0.544] | 0.9 | 81 | This work |
| PCN-222(Mn)/CNT | | -0.60 V vs. RHE [0.494] | 1.1 | 88 | |
| PCN-222(Co)/CNT | | -0.65 V vs. RHE [0.544] | 3.8 | 89 | |
| PCN-222(Ni)/CNT | | -0.80 V vs. RHE [0.694] | 0.8 | 52 | |
| PCN-222(Zn)/CNT | | -0.70 V vs. RHE [0.594] | 1.8 | 92 | |
| [MnBr(2,2-bipyridine)$(CO)_3$]/CNT | 0.5 M $KHCO_3$ | -1.10 V vs. SHE | | 35 | [11] |
| Mn-N-C | 0.1 M $KHCO_3$ | -0.54 V vs. RHE | | 42 | [12] |
| *ortho*-Mn(bpy)$(CO)_3$Br | $CH_3CN$ / 0.1 M $Bu_4NPF_6$ solutions with TFE (20%) | -1.53 V vs. $Fc^{+/0}$ | | 75 | [13] |
| CoPP-PG | 0.1 M $NaClO_4$ | -0.60 V vs. RHE | | 60 | [14] |
| CoPc-P4VP | 0.1 M $NaClO_4$ | -0.73 V vs RHE | | 89 | [15] |
| CoTPP | 0.5 M $KHCO_3$ | -1.05V vs. NHE [0.50] | | 67 | [16] |
| COF-367-Co | 0.5 M $KHCO_3$ | -0.67 V vs RHE [0.55] | | 91 | [17] |
| TTF-Por(Co)-COF | 0.5 M $KHCO_3$ | -0.70 V vs RHE | | 95 | [18] |
| TCPP(Co)/Zr-BTB -PSABA | 0.5 M $KHCO_3$ | -0.77 V vs RHE | 6 | 85 | [19] |
| MOF-1992 | 0.1 M $KHCO_3$ | -0.63 V vs. RHE | | 80 | [20] |
| ZrPP-1-Co@r-GO | 0.5 M $KHCO_3$ | -0.60 V vs RHE | | 82 | [21] |
| $Al_2(OH)_2$TCPP-Co | 0.5 M $K_2CO_3$ | -0.70 V vs. RHE | | 76 | [22] |
| CoPc | 1.0 M $KHCO_3$ | -0.70 V vs. RHE | 3.6 | 62 | [23] |
| CoPc/C | 0.5 M $KHCO_3$ | -0.90 V vs RHE | 28 | 84 | [24] |
| CoPc/N-C-nanorods | 0.1 M $KHCO_3$ | -0.70 V vs RHE | 5 | 85 | [25] |
| CoPc/graphene | 0.1 M $KHCO_3$ | -0.59 V vs RHE | 1.5 | 77 | [26] |
| CoPPc/CNT | 0.5 M $KHCO_3$ | -1.0 V vs NHE | | 76 | [27] |
| CoP/N-rGO | 0.5 M $NaHCO_3$ | -0.70 V vs. RHE | 2 | 80 | [28] |
| Co-N-C | 0.1 M $KHCO_3$ | -0.58 V vs. RHE | | 45 | [29] |
| ZrPP-1-Ni@r-GO | 0.5 M $KHCO_3$ | -0.60 V vs. RHE | | 78 | [21] |
| Ni-$N_4$-C | 0.5 M $KHCO_3$ | -0.81 V vs. RHE | 28.6 | 99 | [30] |
| NiPor-CTF | 0.5 M $KHCO_3$ | -0.90 V vs. RHE | | 97 | [31] |
| Ni-N-C | 0.1 M $KHCO_3$ | -0.80 V vs. RHE | | 88 | [12] |
| Ni@N-CNTs/CP | 0.5 M $KHCO_3$ | -0.76 V vs. RHE | 10.6 | 57 | [32] |
| ]ZrPP-1-Zn@r-GO | 0.5 M $KHCO_3$ | -0.60 V vs. RHE | | 16 | [21] |
| PorZn | 0.1 M TBAPF6 DMF/$H_2O$ | -1.70 V vs. SHE | 2.1 | 95 | [33] |
| ZIF-8 | 0.25 M $K_2SO_4$ | -1.10 V vs. RHE | | 81 | [34] |

## n DFT CALCULATIONS

To reveal the effect of metal centers on $CO_2$RR, we adopted finite cluster calculations for MOFs. The $H_2$-TCPP and M-TCPP were used as calculation models, and $CO_2$RR intermediates (*COOH, *CO) were constructed on this structure. The asterisk (*) represents the active site. All calculations adopt the spin-polarized density functional method within DMol3 code of Materials Studio.[35,36] We selected the Perdew-Burke-Ernzerhof (PBE) of the generalized gradient approximation (GGA) to describe the electron interactions.[37] For transition metals, we employed the DFT Semi-core Pseudopotential (DSPP) method, while for other elements we used the double numerical plus d-functions (DND) basis set.[38,39] The energy, force, and displacement convergence criteria were set as $2 \times 10^{-5}$ Ha, $4 \times 10^{-3}$ Ha/Å, and $5 \times 10^{-3}$ Å in all DFT calculations, respectively. The Gibbs free energy change (ΔG) of every step was obtained by applying the computational hydrogen electrode (CHE) model proposed by Nørskov et al.[40,41] The ΔG and free energy were calculated as:

$$\Delta G_{*COOH} = G_{*COOH} - G_{*} - G_{CO2} - 1/2G_{H2} \quad (1)$$

$$G = E + E_{ZPE} - TS \quad (2)$$

where $E$ is the electronic energy calculated by DFT, $T$ is the temperature; $E_{ZPE}$ and $S$ are the zero point energy and entropy, respectively, estimated under harmonic approximation from the frequency analysis.

**Table S12.** Representation of Frontier Molecular Orbitals in Each Porphyrin Ligand

| | HOMO | | LUMO | |
|---|---|---|---|---|
| Catalyst | Before reduction | After reduction ($e^-$) | Before reduction | After reduction ($e^-$) |
| Mn-TCPP | 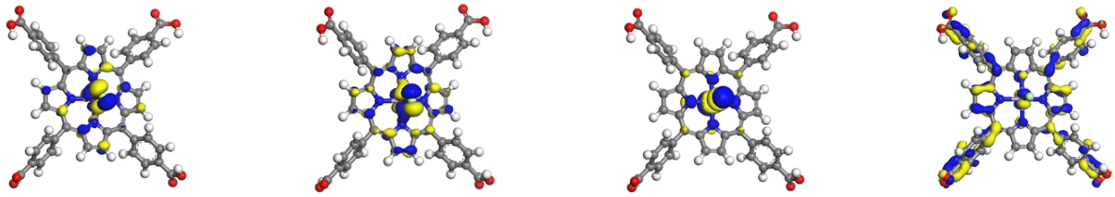 | | | |
| Co-TCPP | 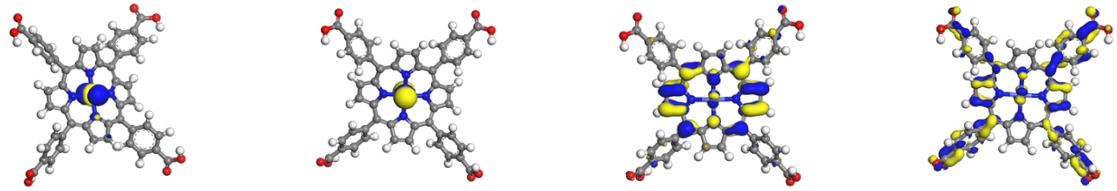 | | | |
| Ni-TCPP | 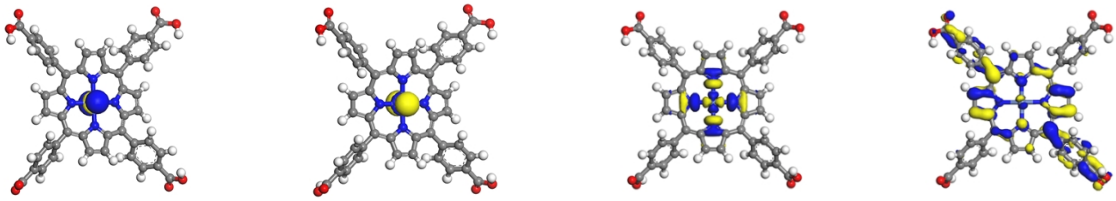 | | | |
| Zn-TCPP | 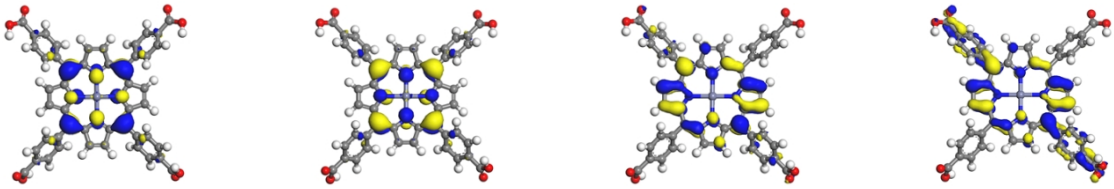 | | | |
| $H_2$-TCPP | 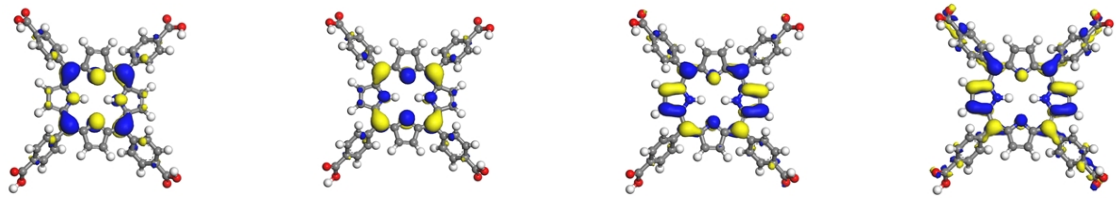 | | | |

**Table S13.** Frontier Molecular Orbital Energies of Each Porphyrin Ligand

| | Before reduction | | | After reduction ($e^-$) | | |
|---|---|---|---|---|---|---|
| Catalyst | $E_{HOMO}$ (eV) | $E_{LUMO}$ (eV) | $\Delta E_{L-H}$ (eV) | $E_{HOMO}$ (eV) | $E_{LUMO}$ (eV) | $\Delta E_{L-H}$ (eV) |
| $H_2$-TCPP | -0.191 | -0.129 | 0.062 | -0.093 | -0.033 | 0.060 |
| Mn-TCPP | -0.177 | -0.141 | 0.036 | -0.059 | -0.036 | 0.023 |
| Co-TCPP | -0.192 | -0.135 | 0.057 | -0.062 | -0.038 | 0.024 |
| Ni-TCPP | -0.196 | -0.136 | 0.060 | -0.091 | -0.036 | 0.055 |
| Zn-TCPP | -0.202 | -0.136 | 0.066 | -0.103 | -0.040 | 0.063 |

## n EXPERIMENTAL SECTION

**Materials and General Method.** Methyl 4-formylbenzoate (99%), pyrrole (99%), propionic acid (99.5%), benzoic acid (99.5%), $ZrCl_4$ (99%), N,N-dimethylformamide (DMF) (99.5%), hydrochloric acid (37%), $MnCl_2·4H_2O$ (99%), $CoCl_2·6H_2O$ (99%), $NiCl_2·6H_2O$ (99%), $ZnCl_2$ (99%), $KHCO_3$ (99.5%) and acetone (99.5%) were from Sinopharm Chemical reagent. CNT was purchased from XFNANO. All chemicals were used as received without further purification. The water used throughout all experiments was deionized with 18.2 MΩ from a Millipore system. Carbon monoxide (99.999%) and hydrogen (99.999%) were used for calibration.

Characterizations of the catalyst were obtained with scanning electron microscopy (SEM) (S-4800II, Japan), field emission transmission electron microscope (HAADF-STEM) (Tecnai G2 F30 S-TWIN, America), and powder X-ray diffraction (PXRD) measurement (AXS D8 ADVANCE, Bruker, German). Low-pressure $N_2$ adsorption measurements (up to 1 bar) were performed on a Micromeritics ASAP 2020 HD88 surface area and a pore size analyzer. The surface elemental compositions of the samples were investigated by X-ray photoelectron spectroscopy (XPS, ESCALAB 250Xi, Thermo Scientific, America). The Fourier transform infrared spectra of the catalysts are collected on Vertex 70 v, Bruker. The UV absorption characteristics were measured on a Cary 5000 UV spectrophotometer.

**Preparation of the Electrodes.** Carbon paper (99.5% carbon, 1 cm × 1 cm) was treated with 6.0 M HCl overnight to remove trace metal impurity, rinsed thoroughly with Milli-Q water, and dried in a vacuum before use.

**Preparation of PCN-222/C and PCN-222(M)/C:** 10.0 mg of PCN-222 and 20.0 mg carbon black (Vulcan XC-72R) were ultrasonically dispersed into 1.0 mL acetone (0.5 wt% Nafion) for 2 h to form a slurry. A 160 $\mu$L of the slurry was dropped on each surface of the carbon paper and then air-dried before use (loading of 3.0 mg $cm^{-2}$). PCN-222(M)/C electrodes were assembled according to the same procedure mentioned above.

**Preparation of PCN-222/CNT and PCN-222(M)/CNT:** 30.0 mg of PCN-222/CNT was ultrasonically dispersed into 2.0 mL acetone (0.5 wt% Nafion) for 2 h to form a slurry. A 300 $\mu$L of the slurry was dropped on each surface of the carbon paper and then air-dried before use (loading of 3.75 mg $cm^{-2}$). PCN-222(M)/CNT electrodes were assembled according to the same procedure mentioned above.

**Electrochemistry and Product Analyses.** Electrochemical reduction of $CO_2$ was performed in an H-type cell with an Ag/AgCl reference electrode and Pt wire was used as the counter electrode. The cathode and anode compartments were separated by a cation exchange membrane (Nafion 117). 0.5 M (60 mL) $KHCO_3$ aqueous solution was used as the electrolyte. Before electrolysis, the electrolyte was pre-saturated with $CO_2$ by bubbling the gas for 30 min (pH 7.4). Current densities were calculated based on the geometric area of the working electrode. A CHI660E electrochemical workstation was used for the electrochemical studies. Electrochemical behaviors were evaluated by the characterization of cyclic voltammetry and chronopotentiometry. All potentials were referred to a reversible hydrogen electrode (RHE). The gas chromatograph (GC, SP-6890) is equipped with columns of TDX-01, GDX502, and PEG-20M, detectors of thermal conductivity detector (TCD), and flame ionization detector (FID) with Ar as a carrier gas. The gaseous products were drawn from the headspace by a gas-tight syringe and injected into the GC. $H_2$, CO, and $CO_2$ with significant amounts were detected by TCD. Standard curves for $H_2$ and CO are shown in Figure S14.

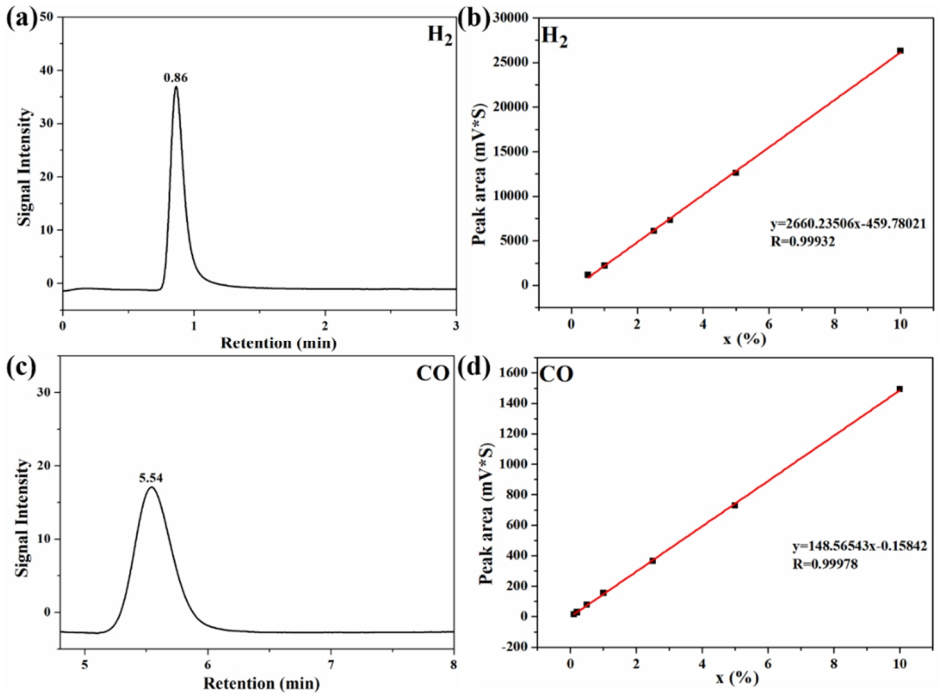


**Figure S14.** Chromatographic peaks (a, c) and standard curves (b, d) for pure hydrogen and CO, established on the TDX-01 column for GC analysis.

## n REFERENCES

(1) L. Wang, P. X. Jin, J. W. Huang, H. D. She, Q. Z. Wang, Integration of copper(II) -porphyrin zirconium metal-organic framework and titanium dioxide to construct Z-scheme system for highly improved photocatalytic $CO_2$ reduction, ACS Sust. Chem. Eng. 7(8) (2019) 15660-15670. https://doi.org/10.1021/acssuschemeng.9b03773

(2) Y. M. Zhao, Y. Z. Dong, F. T. Lu, C. G. Ju, L. Liu, J. Zhang, B. Zhang, Y. Q. Feng, Coordinative integration of a metal-porphyrinic framework and $TiO_2$ nanoparticles for the formation of composite photocatalysts with enhanced visible-light-driven photocatalytic activities, J Mater. Chem. A. 5(29) (2017) 15380-15389. https://doi.org/10.1039/C7TA03840B

(3) M. Aghayan, A. Mahmoudi, S. Sohrabi, S. Dehghanpour, K. Nazaric, N. M. Tabrizi, Micellar catalysis of an iron(III)-MOF: enhanced biosensing characteristics, Anal. Methods. 11(29) (2019) 3175-3187. https://doi.org/10.1039/C9AY00399A

(4) X. D. Zhang, X. T. Lv, F. K. Bi, G. Lu, Y. X. Wang, Highly efficient $Mn_2O_3$ catalysts derived from Mn-MOFs for toluene oxidation: the influence of MOFs precursors, Mol. Catal. 482 (2020) 110701-110709. https://doi.org/10.1016/j.mcat.2019.110701

(5) H. S. Jadhav, A. Roy, G. M. Thorat, W. J. Chung, J. G. Seo, Hierarchical free-standing networks of $MnCo_2S_4$ as efficient electrocatalyst for oxygen evolution reaction, J. Ind. Eng. Chem. 71 (2019) 452-459. https://doi.org/10.1016/j.jiec.2018.12.002

(6) C. G. Pei, H. B. Chen, B. X. Dong, X. Yu, L. G. Feng, Electrochemical oxygen evolution reaction efficiently catalyzed by a novel porous iron-cobalt-fluoride nanocube easily derived from 3-dimensional Prussian blue analogue, J. Power Sources. 424 (2019) 131-137. https://doi.org/10.1016/j.jpowsour.2019.03.089

(7) H. C. Xia, J. N. Zhang, Z. Yang, S. Y. Guo, S. H. Guo, Q. Xu, 2D MOF nanoflake-assembled spherical-micro-structures for enhanced supercapacitor and electrocatalysis performances, Nano Micro. Lett. 9(4) (2017) 43-53. https://doi.org/10.1007/s40820-017-0144-6

(8) W. Kou, Y. X. Zhang, J. Dong, C. H. Mu, L. B. Xu, Nickel-nitrogen-doped three-dimensional ordered macro-/mesoporous carbon as an efficient electrocatalyst for $CO_2$ reduction to CO, ACS Appl. Energy. Mater. 3(2) (2020) 1875-1882. https://doi.org/10.1021/acsaem.9b02324

(9) Y. H. Li, P. F. Liu, C. Z. Li, H. G. Yang, Sharp-tipped zinc nanowires as an efficient electrocatalyst for carbon dioxide reduction, Chem. Eur. J. 24(58) (2018) 15486-15490. https://doi.org/10.1002/chem.201803015

(10) D. W. Feng, Z. Y. Gu, J. R. Li, H. L. Jiang, Z. W. Wei, H. C. Zhou, Zirconium-metalloporphyrin PCN-222: mesoporous metal-organic frameworks with ultrahigh stability as biomimetic catalysts, Angew. Chem. Int. Ed. 124(41) (2012) 10453-10456. https://doi.org/10.1002/ange.201204475

(11) B. Reuillard, K. H. Ly, T. E. Rosser, M. F. Kuehnel, I. Zebger, E. Reisner, Tuning product selectivity for aqueous $CO_2$ reduction with a Mn(bipyridine) -pyrene catalyst immobilized on a carbon nanotube electrode, J. Am. Chem. Soc. 139(41) (2017) 14425-14435. https://doi.org/10.1021/jacs.7b06269

(12) W. Ju, A. Bagger, G. P. Hao, A. S. Varela, I. Sinev, V. Bon, B. R. Cuenya, S. Kaskel, J. Rossmeisl, P. Strasser, Understanding activity and selectivity of metal-nitrogen-doped carbon catalysts for electrochemical reduction of $CO_2$, Nat. Commun. 8 (2017) 944-952. https://doi.org/10.1038/s41467-017-01035-z

(13) S. S. Roy, K. Talukdar, J. W. Jurss, Electro- and photochemical reduction of $CO_2$ by molecular manganese catalysts: exploring the positional effect of second-sphere hydrogen-bond donors, ChemSusChem. 14(2) (2021) 662-670. https://doi.org/10.1002/cssc.202001940

(14) J. Shen, R. Kortlever, R. Kas, Y. Y. Birdja, O. D. Morales, Y. Kwon, I. L. Yanez, K. J. P. Schouten, G. Mul, M. T. M. Koper, Electrocatalytic reduction of carbon dioxide to carbon monoxide and methane at an immobilized cobalt protoporphyrin, Nat. Commun. 6 (2015) 8177-8184. https://doi.org/10.1038/ncomms9177

(15) W. W. Kramer, C. L. McCrory, Polymer coordination promotes selective $CO_2$ reduction by cobalt phthalocyanine, Chem. Sci. 7(4) (2016) 2506-2516. https://doi.org/10.1039/C5SC04015A

(16) A. N. Marianov, Y. J. Jiang, Covalent ligation of Co molecular catalyst to carbon cloth for efficient electroreduction of $CO_2$ in water, Appl. Catal. B: Environ. 244 (2019) 881-888. https://doi.org/10.1016/j.apcatb.2018.11.084

(17) S. Lin, C. S. Diercks, C. J. Chang, N. Kornienko, E. M. Nichols, Y. B. Zhao, A. R. Paris, D. Kim, P. D. Yang, O. M. Yaghi, C. J. Chang, Covalent organic frameworks comprising cobalt porphyrins for catalytic $CO_2$ reduction in water, Science. 349(6253) (2015) 1205-1208. https:// doi.org/10.1126/science.aac6498

(18) Q. Wu, R. K. Xie, M. J. Mao, G. L. Chai, J. D. Yi, S. S. Zhao, Y. B. Huang, R. Cao, Integration of strong electron transporter tetrathiafulvalene into metalloporphyrin-based covalent organic framework for highly efficient electroreduction of $CO_2$, ACS Energy Lett. 5(3) (2020) 1005-1012. https://doi.org/10.1021/acsenergylett.9b02756

(19) X. D. Zhang, S, Z. Hou, J. X. Wu, Z. Y. Gu, Two-dimensional metal-organic framework nanosheets with cobalt-porphyrins for high-performance $CO_2$ electroreduction, Chem. Eur. J. 26(7) (2020) 1604-1611. https://doi.org/10.1002/chem.201904072

(20) R. Matheu, E. G. Puebla, M. A. Monge, C. S. Diercks, J. Kang, M. S. Prevot, X. K. Pei, N. Hanikel, B. Zhang, P. D. Yang, O. M. Yaghi, Three-dimensional phthalocyanine metal-catecholates for high electrochemical carbon dioxide reduction, J. Am. Chem. Soc. 141(43) (2019) 17081-17085. https://doi.org/10.1021/jacs.9b09298

(21) E. X. Chen, J. Yang, M. Qiu, X. Y. Wang, Y. F. Zhang, Y. J. Guo, S. L. Huang, Y. Y. Sun, J. Zhang, Y. Hou, Q. P. Lin, Understanding the efficiency and selectivity of two-electron production of metalloporphyrin-embedded zirconium-pyrogallol scaffolds in electrochemical $CO_2$ reduction, ACS Appl. Mater. Interfaces. 12(47) (2020) 52588-52594. https://doi.org/10.1021/acsami.0c14135

(22) N. Kornienko, Y. B. Zhao, C. S. Kley, C. H. Zhu, D. Kim, S. Lin, C. J. Chang, O. M. Yaghi, P. D. Yang, Metal-organic frameworks for electrocatalytic reduction of carbon dioxide, J. Am. Chem. Soc. 137(44) (2015) 14129-14135. https://doi.org/10.1021/jacs.5b08212

(23) B. H. Hu, W. W. Xie, R. C. Li, Z. W. H. Pan, S. Q. Song, Y. Wang, How does the ligands structure surrounding metal-$N_4$ of Co-based macrocyclic compounds affect electrochemical reduction of $CO_2$ performance, Electrochim. Acta. 331 (2020) 135283-135290. https://doi.org/10.1016/j.electacta.2019.135283

(24) C. He, Y. Zhang, Y. F. Zhang, L. Zhao, L. P. Yuan, J. N. Zhang, J. M. Ma, J. S. Hu, Molecular evidences for metallic cobalt boosting $CO_2$ electroreduction on pyridinic nitrogen, Angew. Chem. Int. Ed. 59(12) (2020) 4914-4919. https://doi.org/10.1002/anie.201916520

(25) H. L. Zhu, Y. Q. Zheng, M. Shui, Synergistic interaction of nitrogen-doped carbon nanorod array anchored with cobalt phthalocyanine for electrochemical reduction of $CO_2$, ACS Appl. Energy Mater. 3(4) (2020) 3893-3901. https://doi.org/10.1021/acsaem.0c00306

(26) J. Choi, P. Wagner, S. Gambhir, R. Jalili, D. R. MacFarlane, G. G. Wallace, D. L. Officer, Steric modification of a cobalt phthalocyanine/graphene catalyst to give enhanced and stable electrochemical $CO_2$ reduction to CO, ACS Energy Lett. 4(3) (2019) 666-672. https://doi.org/10.1021/acsenergylett.8b02355

(27) M. A. Bajada, S. Roy, J. Warnan, K. Abdiaziz, A. Wagner, M. M. Roessler, E. Reisner, A precious-metal-free hybrid electrolyzer for alcohol oxidation coupled to $CO_2$-to-syngas conversion, Angew. Chem. Int. Ed. 59(36) (2020) 15633. https://doi.org/10.1002/anie.202002680

(28) M. H. Zhu, C. X. Cao, J. C. Chen, Y. Sun, R. Q. Ye, J. Xu, Y. F. Han, Electronic tuning of cobalt porphyrins immobilized on nitrogen-doped graphene for $CO_2$ reduction, ACS Appl. Energy Mater. 2(4) (2019) 2435-2440. https://doi.org/10.1021/acsaem.9b00368

(29) F. Q. Pan, H. G. Zhang, K. X. Liu, D. Cullen, K. More, M. Y. Wang, Z. X. Feng, G. F. Wang, G. Wu, Y. Li, Unveiling active sites of $CO_2$ reduction on nitrogen-coordinated and atomically dispersed iron and cobalt catalysts, ACS Catal. 8(4) (2018) 3116-3122. https://doi.org/10.1021/acscatal.8b00398

(30) X. G. Li, W. T. Bi, M. L. Chen, Y. X. Sun, H. X. Ju, W. S. Yan, J. F. Zhu, X. J. Wu, W. S. Chu, C. Z. Wu, Y. Xie, Exclusive Ni-$N_4$ sites realize near-unity CO selectivity for electrochemical $CO_2$ reduction, J. Am. Chem. Soc. 139(42) (2017) 14889-14892. https://doi.org/10.1021/jacs.7b09074

(31) C. B. Lu, J. Yang, S. C. Wei, S. Bi, Y. Xia, M. X. Chen, Y. Hou, M. Qiu, C. Yuan, Y. Z. Su, F. Zhang, H. W. Liang, X. D. Zhuang, Atomic Ni anchored covalent triazine framework as high efficient electrocatalyst for carbon dioxide conversion, Adv. Funct. Mater. 29(10) (2019) 1806884-1806891. https://doi.org/10.1002/adfm.201806884

(32) Z. C. Miao, J. Meng, M. F. Liang, Z. B. Li, Y. Z. Zhao, F. Y. Wang, L. L. Xu, J. L. Mu, S. Q. Zhuo, Jin Zhou, In-situ CVD synthesis of Ni@N-CNTs/carbon paper electrode for electro-reduction of $CO_2$, Carbon. 172 (2021) 324-333. https://doi.org/10.1016/j.carbon.2020.10.044

(33) Y. S. Wu, J. B. Jiang, Z. Weng, M. Y. Wang, D. L. J. Broere, Y. R. Zhong, G. W. Brudvig, Z. X. Feng, H. L. Wang, Electroreduction of $CO_2$ catalyzed by a heterogenized Zn-porphyrin complex with a redox-innocent metal center, ACS Cent. Sci. 3(8) (2017) 847-852. https://doi.org/10.1021/acscentsci.7b00160

(34) X. L. Jiang, H. B. Lia, J. Q. Xiaoc, D. F. Gao, R. Si, F. Yang, Y. S. Li, G. X. Wang, X. H. Bao, Carbon dioxide electroreduction over imidazolate ligands coordinated with Zn(II) center in ZIFs, Nano Energy. 52 (2018) 345-350. https://doi.org/10.1016/j.nanoen.2018.07.047

(35) B. Delley, An all-electron numerical method for solving the local density functional for polyatomic molecules, J. Chem. Phys. 92 (1990) 508-517. https://doi.org/10.1063/1.458452

(36) B. Delley, From molecules to solids with the $DMol^3$ approach, J. Chem. Phys. 113 (2000) 7756-7764. https://doi.org/10.1063/1.1316015

(37) J. P. Perdew, K. Burke, M. Ernzerhof, Generalized gradient approximation made simple, Phys. Rev. Lett. 77 (1996) 3865-3868. https://doi.org/10.1103/PhysRevLett.77.3865

(38) B. Delley, Hardness conserving semilocal pseudopotentials, Phys. Rev. B. 66(15) (2002) 155125-155133. https://doi.org/10.1103/PhysRevB.66.155125

(39) C. Wang, C. Y. Zhu, M. Zhang, Y. Geng, Y. G. Li, Z. M. Su, An intriguing window opened by a metallic two-dimensional lindqvist-cobaltporphyrin organic framework as an electrochemical catalyst for the $CO_2$ reduction reaction, J. Mater. Chem. A. 8(29) (2020) 14807-14814. https://doi.org/10.1039/D0TA04993J

(40) J. K. Nørskov, J. Rossmeisl, A. Logadottir, L. Lindqvist, J. R. Kitchin, T. Bligaard, H. Jónsson, Origin of the overpotential for oxygen reduction at a fuel-cell cathode, J. Phys. Chem. B. 46 (2004) 17886-17892. https://doi.org/10.1021/jp047349j

(41) J. Rossmeisl, A. Logadottir, J. K. Nørskov, Electrolysis of water on (oxidized) metal surfaces, Chem. Phys. 319(1-3) (2005) 178-184. https://doi.org/10.1016/j.chemphys.2005.05.038